Nonlinear Aeroelastic Control of Very Flexible Aircraft Using Model Updating

Yinan Wang[*], Andrew Wynn[†] and Rafael Palacios[‡]
Imperial College, London SW7 2AZ, United Kingdom

A nonlinear modelling strategy is introduced to drive online optimisation-based controllers for trajectory tracking and stabilization of very flexible aircraft. This is achieved thanks to a compact residualised modal projection of the aeroelastic equations of motion, including large (geometrically-nonlinear) wing deflections, that is used to describe the vehicle dynamics. We show that a model-predictive control system can then be built with an internal model based on successive linearisation of the equations of motion around the instantaneous vehicle geometry. Significant improvements in stability against large disturbances and manoeuvrability are demonstrated on numerical simulations of a very flexible flying wing when geometrically-nonlinear effects are included in the internal model of the controller.

Nomenclature

$\mathbf{C}$: Sectional compliance matrix

$\mathbf{e}_1$: Unit vector $(1;0;0)^\top$

$\mathbf{f}$: Sectional internal force vector

H: Number of time steps in control time horizon

$\mathbf{g}$: Graviational acceleration vector

$\mathbf{M}$: Sectional mass matrix

$\mathbf{m}$: Sectional internal moment vector

$\mathbf{q}$: Aeroelastic states in modal basis

$\mathbf{Q}$: Nonlinear operator in state-space aeroelastic system

$\mathbf{R},\mathbf{R}^\dagger$: Similarity transformation matrices for order reduction

$\mathbf{r}$: Displacement in inertial axes

$\mathbf{r}_0$: Reference-node displacement in inertial axes

s: Curvilinear coordinate describing beam location

$\mathbf{s}$: Reduced-order states

t: time

T: current time step

$\mathbf{T}$: Rotation matrix from inertial to local frame

$\mathbf{u}$: Control input vector

V_∞: Forward-flight velocity

$\mathbf{v}$: Local velocity vector

$\mathbf{W}$: MPC weighting matrices

$\mathbf{y}$: Measurement vector

$\boldsymbol{\eta}$: Generalised (modal) forces on the aircraft

$\boldsymbol{\gamma}$: Sectional force strain

$\boldsymbol{\kappa}$: Sectional moment strain

ξ: MPC internal state variable

$\boldsymbol{\phi}_1$: Linear/angular velocity description of mode shape

$\boldsymbol{\phi}_2$: Internal force/moment description of mode shape

$\boldsymbol{\psi}$: Euler angles at the reference node

$\boldsymbol{\omega}$: Local angular velocity vector

$\bullet'$: Derivative w.r.t. s (distance along the beam)

$\dot{\bullet}$: Derivative w.r.t. t (time)

$\tilde{\bullet}$: Cross-product operator

---

[*]Postdoctoral Research Associate, Department of Aeronautics
[†]Senior Lecturer in Control Engineering, Department of Aeronautics
[‡]Reader in Aeronautics, Department of Aeronautics (contact author: rpalacio@imperial.ac.uk), AIAA Member

I.   Introduction

Air vehicles with very high aspect-ratio, but also highly flexible, wings are increasingly considered in order to achieve ambitious targets in aerodynamic efficiency. Their design and analysis has been facilitated by the development of coupled flight dynamic/aeroelastic vehicle models that fully account for geometric nonlinearities, which can play a key role in the vehicle's static and dynamics characteristics [4]. Such models are typically built using composite beam representations of the structures with either thin-strip unsteady aerofoil theory [5, 29] or, more recently, unsteady vortex lattice aerodynamics [32, 19, 10]. A rather comprehensive review of the state of the art in very flexible aircraft dynamic modelling has been recently carried out by Afonso *et al.* [1], and the reader is referred there for further details on the options for computer simulations to support airframe design and performance prediction. The interest here is in the development of model-based guidance and control strategies, specifically tailored to this class of vehicles, that can take advantage of this new nonlinear modelling capability.

Two control problems are particularly relevant for very flexible aircraft. First, noting that such vehicles are highly sensitive to atmospheric conditions, "aggressive" strategies for gust load alleviation can be critical. To date, the focus has been on linear control methods (potentially with gain scheduling [2]) for disturbance rejection that are built on linearisations of the vehicle dynamics around (nonlinear) aeroelastic equilibrium reference conditions [7, 6, 31]. The second problem is trajectory tracking, which may be affected by large changes of wing shape (and the corresponding changes of aerodynamic derivatives) due to the manoeuvre loads. This has been mostly addressed so far using the common assumption of scale separation between an outer navigation loop and an inner (linear) stabilization loop [27, 25, 9]. It is also worth remarking that novel control challenges may be encountered when considering specific mission profiles for very flexible aircraft. For example, trajectory optimization of large solar-powered aircraft defines a resource-constrained problem, in which the available on-board power depends on the instantaneous orientation of the vehicle [18, 16].

All of the previous control strategies were based on linearisation of the vehicle dynamics. Even without encountering saturation, the nonlinear response of very flexible aircraft limits the amplitude of the atmospheric disturbances that can be accommodated by the linear control system in those cases. This has been investigated in a previous work by the authors [31], in which the performance of a linear disturbance rejection controller was studied in response to "1-cos" excitations of very flexible flying wing. For each gust length a maximum gust intensity was found at which the closed-loop system became unstable. Due to the high flexibility and slow speed of the vehicle, this threshold implied that flight was permitted only for severely restricted weather conditions, thus highlighting the need for control strategies that exploit knowledge of the nonlinear vehicle dynamics. While most nonlinear control methodologies are, in general, problem-specific and depend on the structure of the nonlinearities in the system model [28], this work will investigate model-predictive control (MPC), as it poses relatively few requirements on the underlying system [14]. As a result, MPC has been applied to a wide class of nonlinear problems, although its implementation may be computationally

American Institute of Aeronautics and Astronautics

costly if it is to be applied in real time to high-dimensional, rapidly-varying, nonlinear systems. Similar to classical optimal control techniques, the control law in MPC is solved as an optimisation problem. However, this is carried out on-line as opposed to through a predefined gains. Linear MPC with constraints has already been demonstrated on trajectory control of flexible aircraft [13], and gust alleviation using Lidar preview [12].

Nonlinear MPC has also seen wide application in problems with known geometrical nonlinearities, including orbital dynamic control [17, 3] and robotic arm manipulation [11]. However, nonlinear MPC has not been explored for very flexible aircraft, as the existing nonlinear models contain a much larger number of states than the systems described before. To overcome this, in this work, we propose a computationally-efficient strategy for nonlinear aeroelastic simulation of the aircraft dynamics that builds the internal model for the MPC using a successive linearisation approach. This will be achieved through a modal projection of the flexible aircraft dynamic equations, in which the structural geometrical nonlinearities, as well as the aerodynamic and flight dynamic forces are expressed as quadratic nonlinear couplings [30, 31]. The re-linearisation method is selected due to its computational efficiency, where the quadratic form of the nonlinearity in the internal model will also reduce the computational cost associated with the re-linearisation and, although not explicitly sought in the current implementation, enable the proposed MPC to run in real-time. The formulation contains a geometrically-nonlinear intrinsic beam model and a 2D (strip-based) aerodynamic formulation, as well as a flight dynamics model that includes thrust, gust, gravity and control surface effects. Section II outlines the main features of the resulting flexible vehicle dynamics model, in particular, those needed by the nonlinear MPC formulation. Finally, numerical results will be presented in section IV on the application of the nonlinear model-predictive control scheme to a representative flying wing, comparing its performance in disturbance rejection and trajectory tracking with an equivalent linear model-predictive controller.

II.   Aeroservoelastic modelling

Consider a flexible airframe with high-aspect ratio wings, fitted with conventional trailing-edge control surfaces and variable engine thrust. All primary structures will be modelled using geometrically-nonlinear composite beams, with lifting surfaces that deform with the structure and that will be modelled here by strip theory with 2-D unsteady aerodynamics. We will neglect aerodynamic forces on nonlifting bodies. The beam dynamics are described by intrinsic variables, as proposed by Hodges [15], along a reference line, with s being the corresponding curvilinear coordinate defined along the main load paths of the undeformed vehicle. The intrinsic variables are the local inertial velocities (linear, $\mathbf{v}(s,t) \in \mathbb{R}^3$, and angular, $\boldsymbol{\omega}(s,t) \in \mathbb{R}^3$, velocities) and beam sectional forces (internal force $\mathbf{f}(s,t) \in \mathbb{R}^3$ and moment $\mathbf{m}(s,t) \in \mathbb{R}^3$). They are all defined in terms of their components in the local (deformed) reference frame at location s, and shown schematically in Figure 1. Control surfaces are modelled by modifying the local aerodynamic lift, drag and moment coefficients of the lifting surfaces and are described by a vector $\mathbf{u}_\delta(t)$ containing individual control surface deflection angles. The thrust of the engines is finally included as point follower forces of commanded value, which is given by a vector $\mathbf{u}_t(t)$ containing individual engine thrust settings. Details of this

American Institute of Aeronautics and Astronautics

nonlinear aeroservoelastic description can be found in a recent work by the authors [31] and only the main features of the formulation, as well as any changes that were necessary to build the internal models for the MPC, will be outlined here.
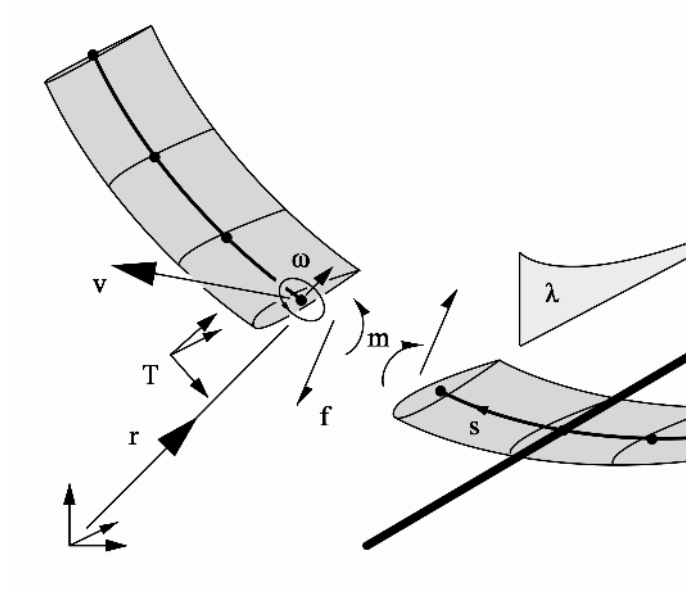

Figure 1. Degrees of freedom used in the aeroelastic formulation in this work.

A. Geometrically-exact beam dynamics in modal coordinates

The geometrically-nonlinear structural dynamics will be described using the linear normal modes of the undeformed and unconstrained airframe beam model in vacuum. This does not introduce *a priori* any additional limitation in the description of the vehicle deformations and kinematics, other than the truncation in modal space associated to a finite-state realisation. The mode shapes are written in terms of the intrinsic variables, that is, the distribution of linear/angular velocities and of internal forces/moments corresponding to a given mode shape in displacements/rotations [30]. This will defined a dual set of basis functions $\phi_{1j}(s) \in \mathbb{R}^6$ and $\phi_{2j}(s) \in \mathbb{R}^6$, for the inertial velocities and internal forces, respectively, each associated with a natural frequency ω_j. Picking the first N modes (with $\omega_j \leq \omega_k$ if $j < k$), the intrinsic variables are then projected as

$$\begin{pmatrix} \mathbf{v}(s,t) \\ \boldsymbol{\omega}(s,t) \end{pmatrix} = \sum_j \phi_{1j}(s) q_{1j}(t), \tag{1a}$$

$$\begin{pmatrix} \mathbf{f}(s,t) \\ \mathbf{m}(s,t) \end{pmatrix} = \sum_j \phi_{2j}(s) q_{2j}(t). \tag{1b}$$

The structural state vector will be then defined as the modal amplitudes, $\mathbf{q}_s = (q_{11}, q_{21}, \ldots, q_{1j}, q_{2j}, \ldots)^\top$. We

choose a convention denoting $\phi_{1j}(s)$, for $j = 1, \ldots, 6$, as the six rigid body modes. Since there are no internal forces associated to such modes, it is therefore $\phi_{2j}(s) = 0$ for $j = 1, \ldots, 6$ and, consequently, the corresponding amplitudes q_{2j} are removed from $\mathbf{q}_s$. The intrinsic beam equations, in terms of these modal coordinates, take the form [31]

$$\dot{\mathbf{q}}_s = \mathbf{A}\mathbf{q}_s + \mathbf{\Gamma}(\mathbf{q}_s)\mathbf{q}_s + \boldsymbol{\eta}_a + \boldsymbol{\eta}_g + \boldsymbol{\eta}_p. \tag{2}$$

Here, the geometrically-nonlinear rigid-body/flexible dynamics of the vehicle is described by a matrix $\mathbf{A}$ (whose coefficients contain the natural frequencies of the undeformed aircraft) and a linear coupling operator $\mathbf{\Gamma}$ that describes all geometrically nonlinear and gyroscopic terms [20]. No structural damping is included in the model. The generalised forces in (2) are the modal projection of the aerodynamic, $\boldsymbol{\eta}_a$, gravitational, $\boldsymbol{\eta}_g$, and propulsion, $\boldsymbol{\eta}_p$, forces, which will be described in the following sections.

From the distribution of inertial velocities we can now obtain, by integration in time from a initial reference shape, the local orientation and position (with respect to an inertial frame) of the reference line as it deforms. The resulting rotation matrix, $\mathbf{T}(s,t) \in \mathbb{R}^{3 \times 3}$, and displacement vector, $\mathbf{r}(s,t) \in \mathbb{R}^3$, are [30]

$$\dot{\mathbf{T}}(s,t) = \mathbf{T}(s,t)\tilde{\boldsymbol{\omega}}(s,t),$$
$$\dot{\mathbf{r}}(s,t) = \mathbf{T}(s,t)\mathbf{v}(s,t), \tag{3}$$

where $\tilde{\bullet}$ indicates the skew-symmetric (or cross-product) operator. In practice, we will only need to integrate (3) at a single reference point to track the flight path. For convenience, we pick that point to be the origin for the curvilinear coordinate $s = 0$. If we define $\mathbf{T}_0(t) = \mathbf{T}(0,t)$ and $\mathbf{r}_0(t) = \mathbf{r}(0,t)$, substitution of (1) into (3) gives

$$\dot{\mathbf{T}}_0 = \mathbf{T}_0\mathbf{N}_1(\mathbf{q}_s),$$
$$\dot{\mathbf{r}}_0 = \mathbf{T}_0\mathbf{N}_2(\mathbf{q}_s), \tag{4}$$

where $\mathbf{N}_1$ and $\mathbf{N}_2$ are linear operators on the q_{1j} components of the structural state vector whose coefficients are the modal amplitudes at $s = 0$, $\phi_{1j}(0)$.

B. Gravitational forces

The components of the modal projection of the gravitational forces in (2) can be written as

$$\eta_{g,j} = \int \phi_{1j}(s)^\top \mathbf{M}(s) \begin{pmatrix} \mathbf{T}^\top(s,t)\mathbf{g} \\ \mathbf{0} \end{pmatrix} ds, \tag{5}$$

where $\mathbf{g}$ is the gravity acceleration vector and $\mathbf{M}(s) \in \mathbb{R}^{6 \times 6}$ is the cross-sectional inertia matrix, which may also include lumped masses. Therefore, as the airframe is assumed to undergo large deformations, it is necessary to com-

American Institute of Aeronautics and Astronautics

pute the local orientation with respect to the Earth axis, $\mathbf{T}(s,t)$ (the same situation occurs for gust loads). In our previous work [31], Eq. (3) was solved at multiple locations along the reference line, to keep the nonlinearity of the overall description second-order. However, this was at the expense of introducing a large number of additional displacement/rotation variables into the state vector, which would hinder the development of real-time control strategies. In this work the instantaneous deformed shape of the aircraft will be obtained, instead, from the spatial integration of the internal forces, which are already computed in (2). For that purpose, we define the moment strains, $\boldsymbol{\kappa}(s,t) \in \mathbb{R}^3$, and force strains, $\boldsymbol{\gamma}(s,t) \in \mathbb{R}^3$, as the energy conjugates of the sectional resultant forces and moments [15], that is,

$$\begin{pmatrix} \boldsymbol{\gamma} \\ \boldsymbol{\kappa} \end{pmatrix} = \mathbf{C} \begin{pmatrix} \mathbf{f} \\ \mathbf{m} \end{pmatrix} = \sum_j \mathbf{C}\boldsymbol{\phi}_{2j}(s)q_{2j}(t), \tag{6}$$

where $\mathbf{C}(s) \in \mathbb{R}^{6 \times 6}$ is the known cross-sectional compliance matrix, which, in general, is a full (symmetric) matrix. The instantaneous position and orientation is obtained from the spatial equivalent (via Kirchoff's analogy) to (3) as

$$\mathbf{T}'(s,t) = \mathbf{T}(s,t)\tilde{\boldsymbol{\kappa}}(s,t), \tag{7a}$$

$$\mathbf{r}'(s,t) = \mathbf{T}(s,t)(\boldsymbol{\gamma}(s,t) + \mathbf{e}_1), \tag{7b}$$

where $\mathbf{e}_1 = (1,0,0)$ and $\bullet'$ indicates the derivative along the beam running direction s. Note that if inextensionality was assumed, that is, $\boldsymbol{\gamma} = \mathbf{0}$, then Eq. (7b) would correspond to the definition of the tangent vector along the deformed beam axis. Substituting (6) into (7), and integrating from $s = 0$ using a piecewise-constant discretisation of the structure [21], we have

$$\mathbf{T}(s) = \mathbf{F}(s,\mathbf{q}_s)\mathbf{T}_0, \tag{8a}$$

$$\mathbf{r}(s) = \mathbf{r}_0 + \mathbf{G}(s,\mathbf{q}_s)\mathbf{T}_0, \tag{8b}$$

where the functions $\mathbf{F}$ and $\mathbf{G}$ are algebraic relations that can be efficiently evaluated at each time step. Substituting (8a) into (5) gives the gravitational forces as a function of the instantaneous aircraft orientation, $\mathbf{T}_0(t)$, and modal amplitudes. Note that this representation is also used by strain-based beam theories [4, 8], although here it is only needed to project gravitational (and gust) loads onto the local deformed reference frame. As will be seen later, this will justify the approximation of (8), which has infinite-order nonlinearities, using a Taylor expansion.

C.   Unsteady aerodynamics

The unsteady aerodynamics are obtained from thin aerofoil theory, using the local velocities of the airframe $(\mathbf{v}, \boldsymbol{\omega})$ with respect to still air to compute the local lift, drag and pitching moment along the reference line in lifting surfaces. Aerodynamic states ($\lambda(s)$ in Figure 1) are introduced to track the unsteady lift history of each aerofoil [24] and are

American Institute of Aeronautics and Astronautics

also projected on the velocity modes. This results in generalized aerodynamic forces given as [31]

$$\boldsymbol{\eta}_a = \mathbf{H}_1(\mathbf{q}_s)\mathbf{q}_s + V_\infty \mathbf{H}_2(\mathbf{q}_a)\mathbf{q}_s + \sum_k \mathbf{H}_{3,k}(\mathbf{q}_s)\mathbf{q}_s u_{\delta k}, \tag{9a}$$

$$\dot{\mathbf{q}}_a = \mathbf{P}_1\mathbf{q}_s - V_\infty \mathbf{P}_2\mathbf{q}_a, \tag{9b}$$

where the modal projection of the aerodynamic loads have been described by the linear operators $\mathbf{H}_1$ and $\mathbf{H}_2$, which depend on the structural and aerodynamic states, respectively. Additionally, the local freestream velocity is approximated by the local forward velocity at the reference point ($s = 0$), which is known from (4), and is referred to as V_∞. The aerodynamic parameters of the lifting surfaces, including lift and drag coefficients, as well as the air density, are incorporated into both operators. The aerodynamic lags are associated to the amplitude of the velocity modes through two constant matrices, $\mathbf{P}_1$ and $\mathbf{P}_2$, in (9b). A third term $\mathbf{H}_3$ is finally included in (9a) to describe the aerodynamic forcing from control surface deflections. It assumes that each individual control surface deflection produces a instantaneous (quasi-steady) linear change in the local aerodynamic lift, drag and moment coefficients. This simple model can easily accommodate atmospheric gusts, as shown in Ref. [31], but that will not be used here.

D. Thrust

The only remaining applied forces on the airframe are the engine thrust forces. Assuming N_p engines, each one will generate a thrust vector given by a prescribed time history of follower point forces $\mathbf{f}_{p,k}$ and moments $\mathbf{m}_{p,k}$, for $k = 1, \ldots, N_p$, on a particular airframe location s_k. The components of the corresponding generalized force in (2) will be then

$$\eta_{p,j} = \sum_k \boldsymbol{\phi}_{1j}(s_k)^\top \begin{pmatrix} \mathbf{f}_{p,k}(t), \\ \\ \mathbf{m}_{p,k} \end{pmatrix} = \mathbf{H}_p\mathbf{u}_p(t) \tag{10}$$

where $\mathbf{H}_p$ is a constant matrix and $\mathbf{u}_p$ is the vector of individual thust settings. The nonlinear ODEs defined by (2), (4), (5), (9), and (10) will be used as a basis for the subsequent model reduction and model-predictive control design, as well as for the numerical simulation of the dynamic response of the flexible aircraft.

III. Nonlinear Model Reduction and Control Design

A. Model Order Reduction

Even with a description on modal coordinates, the (nonlinear) flexible aircraft model formulated above requires a relatively large number of states (typically of order 10^3) for converged time-domain simulations. However, models of much smaller sizes, but that still retain key nonlinear couplings, can also be constructed for the purpose of control synthesis. This will indeed be critical for the success of a MPC architecture, that relies on computationally-efficient internal models of the flexible aircraft dynamics. We first need to re-formulate some parts of the model to better

suit the requirements of order reduction, and subsequently we will derive a small-order description of the nonlinear aeroservoelastic system.

The model-order reduction will be investigated around a trim equilibrium condition. It is defined as the solution the flexible aircraft dynamics such that $\dot{\mathbf{q}}_s = \mathbf{0}$, $\dot{\mathbf{q}}_a = \mathbf{0}$, $\dot{\mathbf{T}}_0 = \mathbf{0}$, and, assuming that the direction of flight is along the y-axis, $\dot{r}_0|_1 = 0$ and $\dot{r}_0|_3 = 0$. This gives reference values for the structural and aerodynamic states, and for the vehicle orientation, as $\mathbf{q}_{se}$, $\mathbf{q}_{ae}$ and $\mathbf{T}_{0e}$, respectively, as well as for the inputs, $\mathbf{u}_{\delta e}$ and $\mathbf{u}_{te}$. Following this, the orientation of the reference node $\mathbf{T}_0$ is expressed by its relative rotation from the trim equilibrium orientation $\mathbf{T}_{0e}$ using Euler angles, $\boldsymbol{\psi}$, as $\mathbf{T}_0 = \mathbf{T}_r(\boldsymbol{\psi})\mathbf{T}_{0e}$ where $\mathbf{T}_r = \mathbf{I}$ at trim. Effectively, for the purpose of derivation of the reduced-order models, the rotation equation in (4) is replaced by

$$\dot{\boldsymbol{\psi}} = f(\boldsymbol{\psi}, \mathbf{q}_s), \tag{11}$$

which will be approximated using a Taylor expansion of order two. We remark that this approximation is only used for the internal model of the controller. The vehicle dynamics are still described by the full-order system of section II.

We can now define the aeroelastic state vector and the control input vector, relative to the trim level, as

$$\mathbf{q} = \begin{bmatrix} (\mathbf{q}_s - \mathbf{q}_{se})^\top & (\mathbf{q}_a - \mathbf{q}_{ae})^\top & \boldsymbol{\psi} \end{bmatrix}^\top, \tag{12a}$$

$$\mathbf{u} = \begin{bmatrix} (\mathbf{u}_\delta - \mathbf{u}_{\delta e})^\top & (\mathbf{u}_t - \mathbf{u}_{te})^\top \end{bmatrix}^\top. \tag{12b}$$

Lastly, to make the MPC problem computationally tractable, we retain only quadratic terms in the gravity forces (5) and ignore the quadratic coupling between structural states $\mathbf{q}_s$ and aerodynamic control inputs $\mathbf{u}_\delta$ in (9a) so that the control input acts on the system only linearly. It will be seen through numerical examples that both approximations on the nonlinear internal model of the MPC do not hinder its performance. Under these assumptions, the aeroelastic system given by (2), (4), and (9), written in terms of the new variable $\mathbf{q}$ effectively reduces to

$$\dot{\mathbf{q}} = (\mathbf{S}_A + \mathbf{Q}(\mathbf{q}))\mathbf{q} + \mathbf{S}_B\mathbf{u}, \tag{13}$$

with $\mathbf{Q}$ a linear operator. Additionally, we define sensor measurements involving either velocities, forces and strains at different locations along s, as well as rotations or displacements of the body-fixed reference frame, modelled as a linear combination of the states $\mathbf{q}$ according to (1) and will result in the measurement matrix $\mathbf{S}_C$ and the output vector $\mathbf{y}$,

$$\mathbf{y} = \mathbf{S}_C\mathbf{q}. \tag{14}$$

Equations (13) and (14) form a closed-form description of the dynamics of a HALE aircraft with quadratic non-

linearities

$$\begin{pmatrix} \dot{\mathbf{q}} \\ \mathbf{y} \end{pmatrix} = \begin{pmatrix} \mathbf{S}_A + \mathbf{Q}(\mathbf{q}) & \mathbf{S}_B \\ \mathbf{S}_C & \mathbf{0} \end{pmatrix} \begin{pmatrix} \mathbf{q} \\ \mathbf{u} \end{pmatrix}. \tag{15}$$

The next step is to reduce the dimension of this nonlinear dynamic model so that it can be implemented as an on-line optimisation scheme. This process starts by carrying out a balanced transformation of the linear system at the reference conditions (where $\mathbf{Q}(\mathbf{q}) = 0$). This results in a similarity transformation that will be written as

$$\mathbf{R} : \mathbb{R}^{N_q} \to \mathbb{R}^{N_s}, \quad \mathbf{q} \mapsto \mathbf{Rq}, \tag{16}$$

where $N_s \ll N_q$, and $\mathbf{R}$ is the projection matrix with pseudo-inverse $\mathbf{R}^\dagger$ satisfying $\mathbf{RR}^\dagger = \mathbf{I}$. This linear transformation is then applied to the nonlinear state equations (15), which results in

$$\begin{pmatrix} \dot{\mathbf{s}} \\ \mathbf{y} \end{pmatrix} = \begin{pmatrix} \mathbf{RS}_A\mathbf{R}^\dagger + \mathbf{RQ}(\mathbf{R}^\dagger\mathbf{s})\mathbf{R}^\dagger & \mathbf{RS}_B \\ \mathbf{S}_C\mathbf{R}^\dagger & \mathbf{0} \end{pmatrix} \begin{pmatrix} \mathbf{s} \\ \mathbf{u} \end{pmatrix} =: \begin{pmatrix} \mathbf{S}_{rA} + \mathbf{Q}_r(\mathbf{s}) & \mathbf{S}_{rB} \\ \mathbf{S}_{rC} & \mathbf{0} \end{pmatrix} \begin{pmatrix} \mathbf{s} \\ \mathbf{u} \end{pmatrix}, \tag{17}$$

where $\mathbf{s} \in \mathbb{R}^{N_s}$ is the reduced-order state, which provides an approximation of the full system via $\mathbf{q} \approx \mathbf{R}^\dagger\mathbf{s}$. Furthermore, the nonlinear term in (17) can be efficiently expressed if we write $\mathbf{Q}(\mathbf{q})\mathbf{q} = Q_{ijk}q_jq_k$ to give

$$\mathbf{Q}_r(\mathbf{s})\mathbf{s} = \mathbf{RQ}(\mathbf{R}^\dagger\mathbf{s})\mathbf{R}^\dagger\mathbf{s} = R_{im}Q_{mns}R_{nj}^\dagger s_j R_{sk}^\dagger s_k = \left(R_{im}Q_{mns}R_{nj}^\dagger R_{sk}^\dagger \right) s_j s_k, \tag{18}$$

where, noting that the size of $\mathbf{Q}_r$ will be small, the coefficients in the parenthesis can be precomputed at only a moderate cost. For a time step Δt, a discrete-time linear approximation of the nonlinear reduced-order system (17) with states $(\mathbf{s}_i, \mathbf{u}_i, \mathbf{y}_i)$ is formed by linearising the quadratic nonlinearity about $\mathbf{s}_i$ and fixing the control input $\mathbf{u}(t) \equiv \mathbf{u}_i$ over each time step $t \in [i\Delta t, (i+1)\Delta t]$ to give

$$\mathbf{s}_{i+1} = \left[\mathbf{I} + \tilde{\mathbf{A}}(\mathbf{s}_i)^{-1} \left(e^{\Delta t\tilde{\mathbf{A}}(\mathbf{s}_i)} - \mathbf{I} \right) (\mathbf{S}_{rA} + \mathbf{Q}_r(\mathbf{s}_i)) \right] \mathbf{s}_i + \tilde{\mathbf{A}}(\mathbf{s}_i)^{-1} \left(e^{\Delta t\tilde{\mathbf{A}}(\mathbf{s}_i)} - I \right) \mathbf{S}_{rB}\mathbf{u}_i, \tag{19}$$

where $\tilde{\mathbf{A}}(\cdot) : \mathbb{R}^{N_s} \to \mathbb{R}^{N_s \times N_s}$ is the linear operator such that $\tilde{\mathbf{A}}(\mathbf{x})\mathbf{y} = \mathbf{S}_{rA}y + \mathbf{Q}_r(\mathbf{x})\mathbf{y} + \mathbf{Q}_r(\mathbf{y})\mathbf{x}$ for any $\mathbf{x}, \mathbf{y} \in \mathbb{R}^{N_s}$. Consequently, we can write the linearised discrete time approximation in the form

$$\begin{pmatrix} \mathbf{s}_{i+1} \\ \mathbf{y} \end{pmatrix} = \begin{pmatrix} \overline{\mathbf{S}}_{rA,i} & \overline{\mathbf{S}}_{rB,i} \\ \mathbf{S}_{rC} & \mathbf{0} \end{pmatrix} \begin{pmatrix} \mathbf{s}_i \\ \mathbf{u}_i \end{pmatrix}, \tag{20}$$

where $\overline{\mathbf{S}}_{rA,i} := \left[\mathbf{I} + \tilde{\mathbf{A}}(\mathbf{s}_i)^{-1} \left(e^{\Delta t\tilde{\mathbf{A}}(\mathbf{s}_i)} - \mathbf{I} \right) (\mathbf{S}_{rA} + \mathbf{Q}_r(\mathbf{s}_i)) \right]$ and $\overline{\mathbf{S}}_{rB,i} := \tilde{\mathbf{A}}(\mathbf{s}_i)^{-1} \left(e^{\Delta t\tilde{\mathbf{A}}(\mathbf{s}_i)} - \mathbf{I} \right) \mathbf{S}_{rB}$.

B. Model-Predictive Control Formulation

The model-predictive control scheme considered in this work is a time-invariant receding-horizon control law $\mathbf{u}_T :=$ $\mathcal{K}(\mathbf{s}_T, \mathbf{y}^{ref}(\cdot|T), \mathbf{u}^{ref}(\cdot|T), \mathbf{u}_{T-1})$ which defines, at each control time step $T \geq 1$, the control input $\mathbf{u}_T$ based upon knowledge of the current state $\mathbf{s}_T = \mathbf{Rq}(T\Delta t)$ and chosen reference values[a]

$$\mathbf{y}^{ref}(\cdot|T) = \{\mathbf{y}^{ref}(i|T)\}_{i=T}^{T+H}, \qquad \mathbf{u}^{ref}(\cdot|T) := \{\mathbf{u}^{ref}(i|T)\}_{i=T}^{T+H-1},$$

of the output and input over a prediction horizon of length $H \in \mathbb{N}$. In particular, $u_T := \nu_T^*$ is defined in terms of the solution to the on-line optimization problem

$$\min_{\boldsymbol{\xi}_i, \boldsymbol{\nu}_i} \sum_{i=T}^{T+H-1} \left|\left|\mathbf{S}_{rC}\boldsymbol{\xi}_i - \mathbf{y}^{\text{ref}}(i|T)\right|\right|_{\mathbf{W}_1}^2 + \left|\left|\boldsymbol{\nu}_i - \mathbf{u}^{ref}(i|T)\right|\right|_{\mathbf{W}_2}^2 + \left|\left|\boldsymbol{\nu}_i - \boldsymbol{\nu}_{i-1}\right|\right|_{\mathbf{W}_3}^2 \tag{21a}$$

$$+ \left|\left|\mathbf{S}_{rC}\boldsymbol{\xi}_{T+H} - \mathbf{y}^{\text{ref}}(T+H|T)\right|\right|_{\mathbf{W}_4}^2$$

subject to

$$\boldsymbol{\xi}_{i+1} = \overline{\mathbf{S}}_{rA,T}\boldsymbol{\xi}_i + \overline{\mathbf{S}}_{rB,T}\boldsymbol{\nu}_i, \qquad i = T, \ldots, T+H-1, \tag{21b}$$

$$\boldsymbol{\xi}_T = \mathbf{s}_T, \tag{21c}$$

$$\boldsymbol{\nu}_{T-1} = \mathbf{u}_{T-1}, \tag{21d}$$

with weighting matrices for outputs $\mathbf{W}_1$, inputs $\mathbf{W}_2$, input rates $\mathbf{W}_3$ and terminal cost $\mathbf{W}_4$ where $||\mathbf{v}||_{\mathbf{W}}^2 = \mathbf{v}^\top \mathbf{W} \mathbf{v}$. We note that the output cost (weighted by $\mathbf{W}_1$) is equivalent to a state cost of $\mathbf{S}_{rC}^\top \mathbf{W}_1 \mathbf{S}_{rC}$ in a standard MPC problem. Information is retained between subsequent MPC optimizations via imposition of the constraint $\boldsymbol{\nu}_{T-1} = \mathbf{u}_{T-1}$ which appears in the input-rate component of the cost function. The evolution of states at each time step, i.e. the internal model, is described by (21b) which is given by evaluating Eq. (20) at the current time step, T. Initial knowledge of the reduced states at the current time is given in equation (21c), where full-state feedback is assumed, meaning that we do not consider state estimation in this work, and that the full specification of the MPC problem consists of (16) and (21).

Effectively, this specification of MPC assumes that the re-linearised state transition relation at each time T, $\overline{\mathbf{S}}_{rA,T}$, can be used to approximate the dynamics for the duration of the optimisation window. The optimisation itself is typically solved as a convex optimisation problem [26], however, in this exploratory work it will be further assumed that the saturation limits are never reached (which will be checked *a posteriori* in the numerical examples below). This removes the need for inequality constraints and, as a result, the optimal solution can be solved via a one-step quadratic programme. Despite the assumption of full-state feedback, it is nonetheless convenient to penalise only particular chosen outputs $\mathbf{S}_{rC}\boldsymbol{\xi}_i$ of the state in the cost (21a). The rationale for this choice is that a desired output trajectory $\mathbf{y}^{\text{ref}}(\cdot|T)$ must also be calculated at each time T and that output trajectories are significantly simpler to compute than

---

[a]The notation $(\cdot|T)$ indicates a quantity that is defined at time T to emphasise that reference trajectories may be time-dependent.

American Institute of Aeronautics and Astronautics

full-state trajectories. This will be further discussed through relevant examples in the next section.

IV.   Numerical Results

A.   Test Case Description

A nonlinear aeroelastic vehicle in free flight is now considered to demonstrate MPC control design and closed-loop nonlinear dynamic simulation. The aircraft is the 72m-span high-aspect ratio flying wing model originally defined by Patil and Hodges [23] and subsequently used by other studies [32, 29, 31], for which the main geometrical features are shown in Figure 2 and the main properties are shown in Table 1. The airframe has a flat, straight midsection and an outer section with $10°$ dihedral. Three vertical fins are placed below the midsection and thrust is provided by five propellers mounted forward of the wing. In this work, a payload of 227 kg is placed at the central pod, for which the open-loop configuration is dynamically unstable at sea level and the nominal airspeed, 12.2 m/s [31].
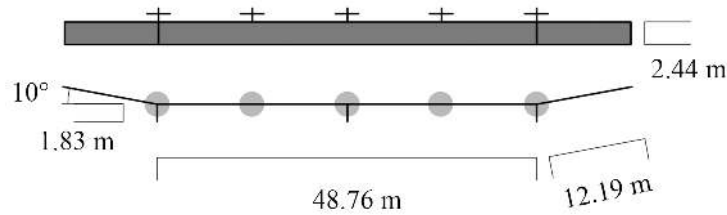
Figure 2.   Geometric configuration of the flying wing.

Elastic/reference axis	25% chord
Aerodynamic centre	25% chord
Centre of gravity	25% chord
GJ	$1.65 \times 10^5 \text{Nm}^2$
EI_2	$1.03 \times 10^6 \text{Nm}^2$
EI_3	$1.24 \times 10^7 \text{Nm}^2$
m	8.93kg/m
I_{11}	4.15 kg m
I_{22}	0.69 kg m
I_{33}	3.46 kg m
Wing $c_{l\alpha}$	2π
Wing $c_{l\delta}$	1
Wing c_{d0}	0.01
Wing c_{m0}	0.025
Wing $c_{m\delta}$	-0.25
Pod $c_{l\alpha}$	5
Pod c_{d0}	0.02
Pod c_{m0}	0

Table 1. Relevant properties of the flying wing [29].

American Institute of Aeronautics and Astronautics

A standard (linear) finite-element beam model is built to obtain the linear normal modes of the airframe. It contains 20 elements for each side of the central section, 10 elements for the outer section and a single rigid element each for each of the three fins under the wing. The mode shapes are then transformed [30] into intrinsic variables to obtain the basis ϕ_1 and ϕ_2 used in (2). The aerofoil coefficients in Table 1 and the five follower forces at the engines lead finally to the influence coefficients, $\mathbf{H}$, defined in Eqs. (9) and (10). The resulting full-order system has 1966 states. A comparison against the literature of full-model results for this configuration can be found in our previous work [31].

B.   Nonlinear Reduced-Order Aeroelastic Model

The full-order system is first cast into the form of (13), with the six control inputs and ten measurement channels specified in Tables 2 and 3, respectively. Figure 3 shows the combinations of flap deflections and thrust that define each of the input channels in Table 2. All measurements are taken at the centre node (i.e. located at the midpoint, directly above the central pod) of the flying wing and all inputs and measurements are defined by their incremental value with respect to trim.
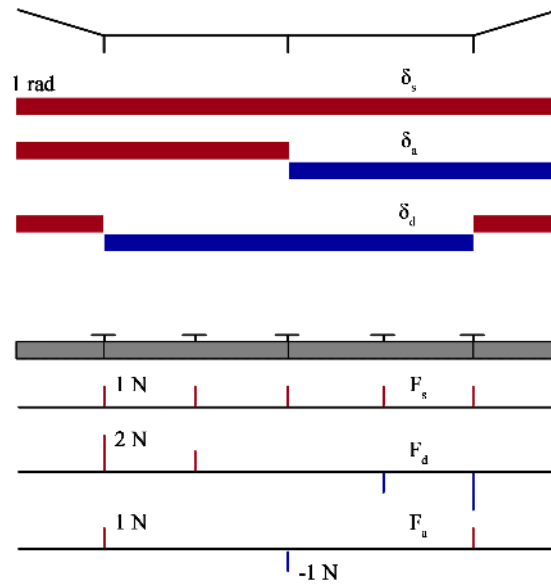
Figure 3.   Control inputs on the flying wing.

Ranking the balanced states of the linear aeroelastic system using their Hankel singular values, as few as 15 states can be seen to be necessary to capture the main linear input/output dynamics (including both longitudinal and lateral dynamics). The transformation (16) is then carried out and Figure 4 shows two characteristic Bode plots of the resulting system: first, the response in rigid-body normal velocity v_3 (in body-fixed axes) to uniform flap input, δ_s, (a longitudinal response); and, second, the response to yaw rate, ω_3, to antisymmetric flap input, δ_a (as an example of

#	Definition	Symbol	Units
1	Uniform flap deflection	δ_s	rad
2	Differential flap deflection	δ_d	rad
3	Uniform thrust action	F_s	N
4	Differential thrust action	F_d	N
5	Antisymmetric flap deflection	δ_a	rad
6	Antisymmetric thrust action	F_a	N

Table 2. Control input channels on the flying wing model.

#	Definition	Symbol	Units
1	Symmetric root bending moment	M_2	kNm
2	Body-fixed longitudinal velocity	v_2	m/s
3	Body-fixed normal velocity	v_3	m/s
4	Body-fixed pitch rate	ω_1	rad/s
5	Rigid-body pitch (in $z - y' - x''$ Euler angle)	ψ_1	rad
6	Antisymmetric root torsion moment	M_1	kNm
7	Body-fixed sideslip velocity	v_1	m/s
8	Body-fixed roll rate	ω_2	rad/s
9	Body-fixed yaw rate	ω_3	rad/s
10	Rigid-body roll (in $z - y' - x''$ Euler angle)	ψ_2	rad

Table 3. Measurement channels on the flying wing model.

lateral response). Both indicate that low-frequency dynamics in the bandwidth of interest (below 1 rad/s) are indeed well preserved with the first 15 balanced states. The poles of the linear parts of the full- and reduced-order system with 15 states can be finally seen in Figure 5, where the unstable pair corresponds to the phugoid mode.

a) δ_s to v_3 (**symmetric**)

b) δ_a to ω_3 (**antisymmetric**)
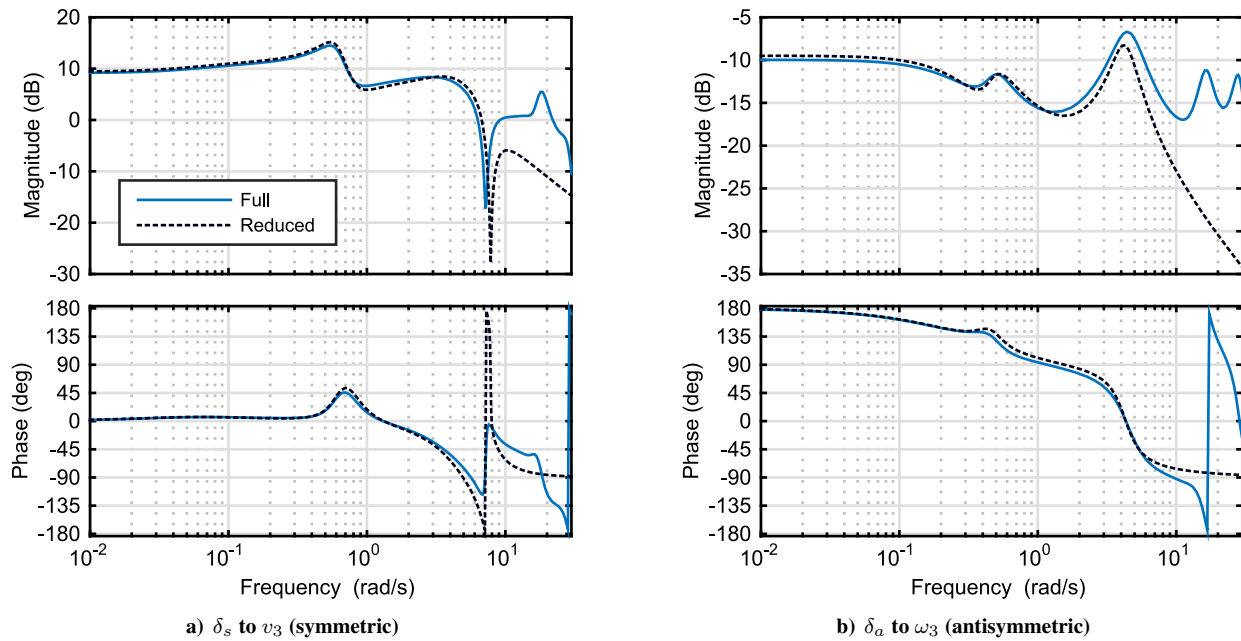
Figure 4.   Sample Bode plots of for full linear system and reduced-order system with 15 balanced states.
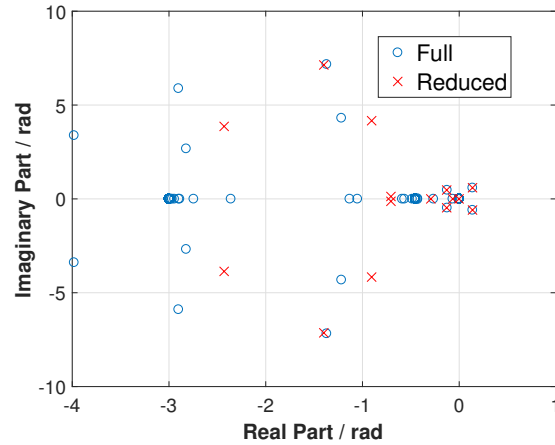
Figure 5. Poles near the origin of the full- and reduced-order systems. Unstable pair corresponds to the phugoid mode.
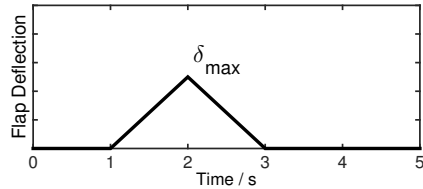

Figure 6. Flap input profile for the open-loop test cases.

Once the linearised system at the trim conditions has been characterised, the corresponding reduced-order nonlinear aeroelastic model (20) is obtained. Two nonlinear reduced-order models are considered, a first one with 15 states, which was seen to be sufficient for linear analysis, and a larger one with the first 50 states obtained in the linear balancing process. Comparisons are made between the time-domain open-loop response to symmetric and antisymmetric flap excitations of both reduced-order models and the full-order system to explore the effect of system size. The time-history of the flap inputs is always as shown in Figure 6. First, a symmetric excitation in flap input, δ_s in Figure 3, with $\delta_{max} = 2$ deg is given to the aircraft in its trim state, for which the response is shown in Figure 7 in terms of in-plane and out-of-plane velocity components at the midpoint of the wing, as well as the instantaneous pitch angle and bending moment resultant at that point. Results compare the full-order and reduced nonlinear systems, as well a reduced linear system with the same 15 states. The response from the linearised full-order system is indistinguishable from the 15 state linear system and it is not shown. Clearly, the symmetric response is dominated by the unstable phugoid oscillations. The nonlinear ROMs demonstrate better agreement with the full model than the linear ROM, with the 15-state model capturing well the rigid-body dynamics, and the 50-state model improving the characterisation of the structural effects. Indeed, the results with 50 states match very well those obtained from the full-system simulations.

Figure 8 shows the response to antisymmetric flap excitation, δ_a, defined as in Figure 3 and with $\delta_{max} = 10$ deg. The vehicle displays here a nonlinear coupling between its antisymmetric and symmetric dynamics, which is
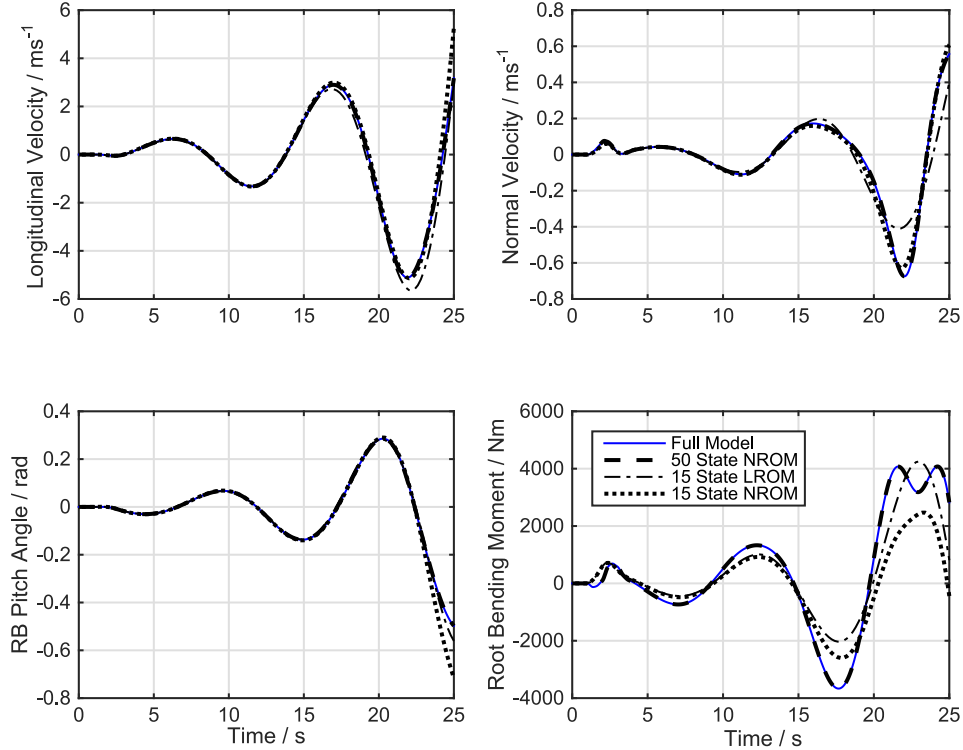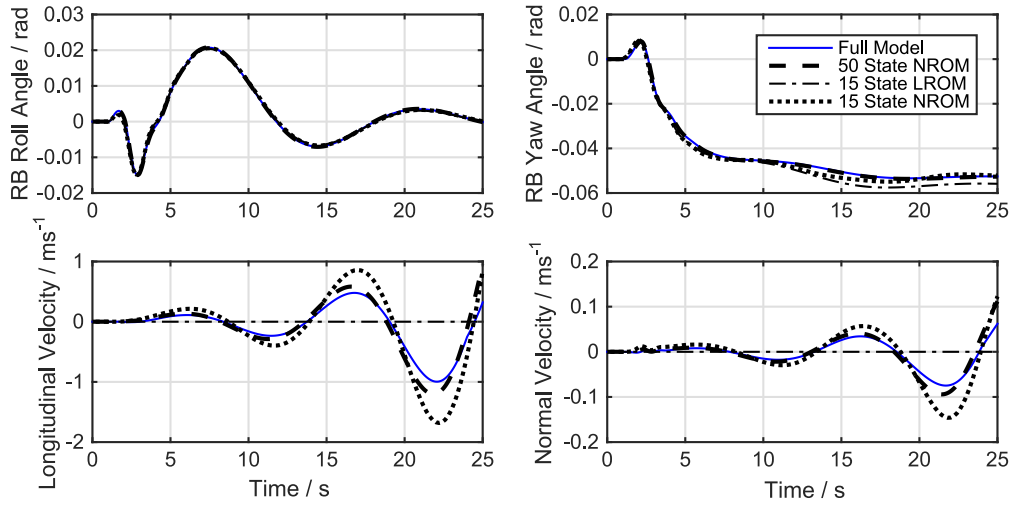
Figure 7. Dynamic response of full- and reduced-order models to a symmetric flap input δ_s with profile shown in Figure 6 and $\delta_{max} = 2°$.

not captured by the linear model. First, note that the lateral response (yaw and roll angles are presented in Figure 8) is captured well by all models, as it is dominated by the linearised dynamics – noting that the linearisation was done around the deformed aircraft in trim, which displays a high effective dihedral angle. As the vehicle rolls, there is a change in lift that introduces a (nonlinear) coupling with the longitudinal aircraft dynamics, which then grows in amplitude because of the unstable phugoid. This is shown by the two longitudinal components of the velocity at the wing midpoint in body-fixed axes, also included in Figure 8. The linearised ROM, however, does not capture the symmetric-antisymmetric coupling and no response is seen in the those symmetric measurements. The 50-state nonlinear ROM captures the coupling with the smallest error of all the monitored variables, whereas the 15-state ROM also captures the coupling but with a larger error. In what follows, we will consider that the 50-state description is suitable for simulation (although, unless otherwise state, all our flight simulations are carried out on the full-size model), and that the 15-state is suitable as internal model for control. A further exploration on a large range of flight scenarios would provide tighter bounds for the size of both models, but this was deemed sufficient to highlight the features of the method in this work.

Figure 8. Dynamic response of full- and reduced-order models to an asymmetric flap input δ_a with profile shown in Figure 6 and $\delta_{max} = 10°$.

C.   MPC Closed-Loop Performance

1.   Design and Implementation

The model-updating MPC described in Section III.B is now implemented for disturbance rejection on the flying wing model. First, the size of the reduced-order nonlinear internal model needs to be chosen, which is done through a trade-off between accuracy, in particular, the ability to capture the dominant nonlinear couplings in the vehicle response, and computational performance, so as to allow solution of the optimization at a faster rate that the full-system simulation. We note that our current implementation of the control algorithm has not been optimized for performance and a real-time solution has not yet been attempted. From the results in the previous section, a 15-state reduced-order nonlinear model was chosen and will be used throughout this section. Further gains against linear control schemes would still be possible with a further optimized controller architecture and a larger internal model.

The internal model of the MPC is therefore the 15-state model defined above, with a time step $\Delta t = 0.2$ s and a 3-second horizon ($H = 15$ in (21a)). The controller itself is also assumed to operate at an interval of 0.2 s (i.e. the same as the internal time step) with a zero-order hold, whereas the full-order model operates with an adaptive time step defined by the Runge-Kutta solver (typically in the order of 0.01 s). The nonlinear internal model is used to compute an updated linear model only at each new time step where the MPC is evaluated, and each MPC optimization is performed using a fixed linearized model for the duration of the prediction horizon. Full-state feedback is assumed, with the current reduced-order states $\mathbf{s}_T$ computed from the full system state $\mathbf{q}(T\Delta t)$ via the constant projection matrix $\mathbf{R}$ in (16). After a numerical investigation, the weighting matrices have been chosen as $\mathbf{W}_1 = 20 \operatorname{diag}(1, 1, 1, 1, 10, 1, 1, 1, 1, 10)$ on the outputs, $\mathbf{W}_2 = \frac{1}{3} \operatorname{diag}(1, 1, 0.1, 0.1, 1, 0.1)$ on the inputs, $\mathbf{W}_3 = 3 \operatorname{diag}(20, 20, 0.05, 0.05, 20, 0.05)$ on the input rates, and terminal constraints $\mathbf{W}_4 = 300\mathbf{W}_1$, with input and output channels defined as in Tables 2 and 3, respectively (e.g., the larger weights in the output channels are on the instantaneous pitch and roll angles).

American Institute of Aeronautics and Astronautics

2. Disturbance Rejection

The closed-loop disturbance rejection characteristics are first investigated. To allow a direct characterization of the nonlinear effects, the excitation will be introduced as a change of the initial conditions. In particular, an initial amplitude of the unstable phugoid mode is defined, with magnitude varying from $q_{11}(0) = 0.2$ (for which nonlinear effects are small) to $q_{11}(0) = 2.0$, which corresponds to a 1.2 m/s change in forward velocity (a 16.4% change from the reference velocity). The regulation characteristics of the nonlinear MPC are compared against an equivalent linear MPC (i.e., where the state transition matrix $\overline{\mathbf{S}}_{rA,0}$ obtained at the trim linearisation, and all other settings in the controller, remain unchanged).
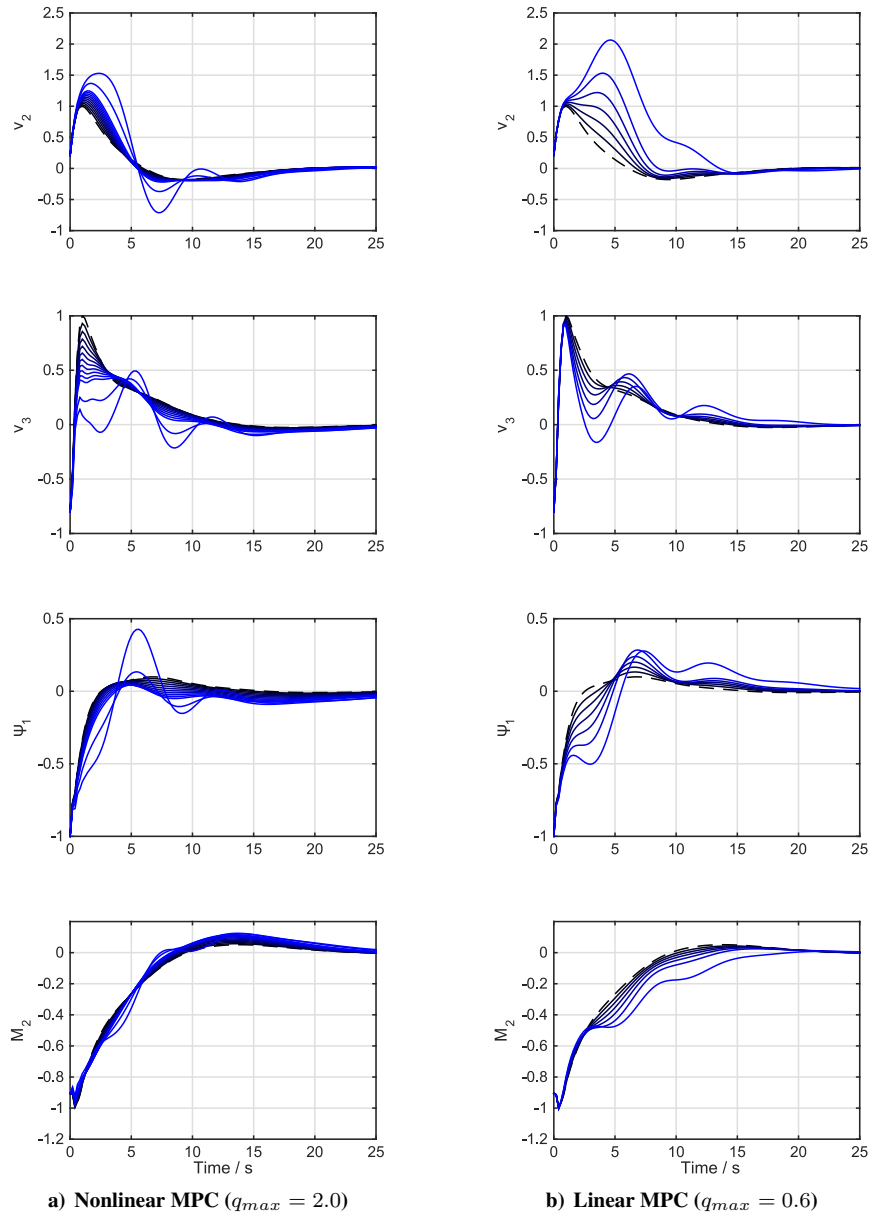
Figure 9. State variables (normalised by corresponding linear response) at wing midpoint for $q_{11}(0)$ from .2 (darker) to q_{max} (lighter). Dashed lines: linearised vehicle model.

Figure 9 compares the closed-loop response of the full-order model when driven by either the linear and nonlinear controllers. Results are presented in terms of body-fixed velocities at the wing midpoint, the instantaneous pitch angle at that point, and wing root bending moment. For the nonlinear controller, results correspond to $q_{11}(0) = \{0.2, 0.3, \cdots 1.0, 1.5, 2.0\}$, while for the linear controller they are limited to $q_{11}(0) = \{0.2, 0.3, \cdots 0.6\}$, as the closed-loop system with this controller diverges for higher amplitudes of the excitation. Only results up to the stability limit are shown. To facilitate the comparison with increasing initial amplitudes, all results have been normalised by the maximum value in the corresponding linear closed-loop system (that is, with both linear system and linear control). As a reference, the linear-system results have been included, and the vertical axes are normalised such that

the maximum amplitude in that problem is 1. This normalisation allows for direct observation of the nonlinear effects in the closed-loop system. In all cases, nonlinear effects are initially negligible, but they soon start to create differences in performance between the linear and nonlinear controllers. As it can be seen, the body-fixed longitudinal velocity (v_2) with the nonlinear controller scales nearly linearly until $q_{11}(0) = 1$, while the linear controller (for which results are shown for a smaller range of initial conditions) has a large overshoot before it is brought down. Similar behaviour is observed in the time-history of the pitch angle. The body-fixed vertical shows even starker behaviour, as the nonlinear controller reduces up to 50% the peak values observed on the corresponding linear system. The linear controller on the nonlinear system is not able to achieve this. Finally, it is worth noting that root bending moments remain rather similar for both controllers, thus suggesting that dynamic loads in this configuration are mostly dominated by the linear system response.

Figure 10 shows the corresponding time-history in all four longitudinal input control channels for both controllers under the same set of initial conditions. As before, the results are normalised with the peak value of the corresponding linear simulation (linear controller with linear model, for which the results are also included in the figures with dash lines). Unit value in the y axes therefore corresponds to the maximum obtained the corresponding linear model and the differences between continuous curves and the dash curve therefore quantify the effects of the system nonlinearities as the amplitude increases (for linear models they would collapse to the dash line). It is also important to monitor the absolute values of the input signals, to ensure that are within realistic bounds. In particular, for $q_{11}(0) = 1$, which is a very large excitation, the maximum and minimum values for the control inputs on the nonlinear MPC (Figure 10a) are $-16.0° < \delta_s < 0.4°$, $8.1° < \delta_d < 0.4°$, $-3.2\text{N} < F_s < 31.0\text{N}$ and $-10.7\text{N} < F_d < 0.8\text{N}$. As it was discussed, no saturation has been included in the controller, but, as it can be seen, all results up to $q_{11}(0) = 1$ are within the normal bounds of physical actuators.

From a comparison between both sets of results, it can be seen that, for a given excitation, the closed-loop dynamic response from the nonlinear MPC is substantially less dependent on the strength of initial excitation, that is, the deviation from the linear results occurs more gradually as the amplitude increases. As a result, the nonlinear MPC is able to stabilise the aircraft when subjected to much larger initial disturbances. This is quantified in Figure 11, which shows the stability regions of both the linear and nonlinear MPC when subject to simultaneous initial excitations in longitudinal velocity (v_2) and root bending moment (M_2). The stability of the nonlinear system is established here by decreasing oscillation amplitudes in the last half of a 25-s simulation. Again, a significant expansion of the parameter space corresponding to stable closed-loop dynamics is seen when model re-linearisation is used within the MPC optimization problem. Typically, the nonlinear stability boundary is the result of the differences between the reduced-order and full models, which become more significant as the system moves away further from equilibrium. While the convergence of the nonlinear system would be somehow reduced for the larger amplitudes if control input saturation was implemented (although all inputs were checked to be within acceptable bounds in our simulations), some redesign
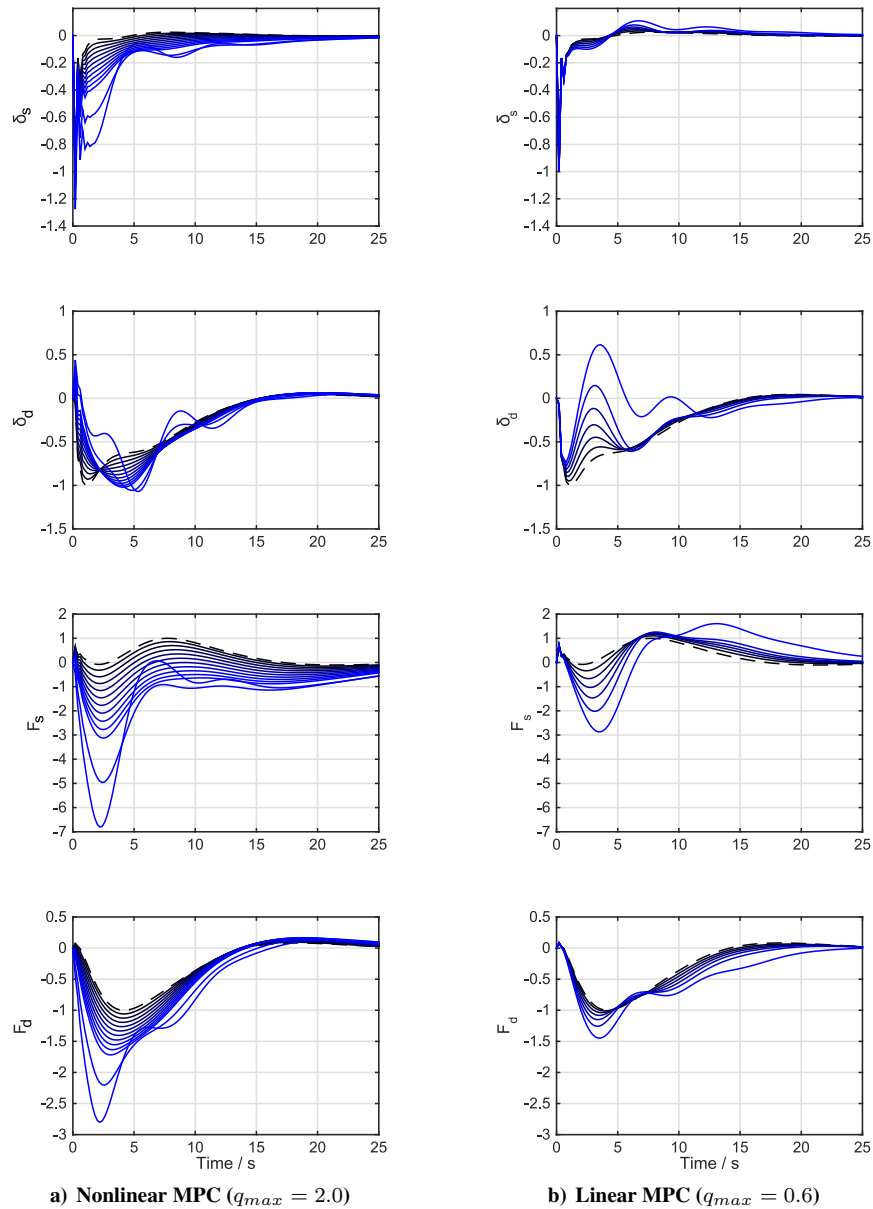
Figure 10. Normalised control actions in response to initial conditions on $q_{11}(0)$ from .2 (darker) to q_{max} (lighter). Dashed lines: linearised vehicle model.

of both actuator geometry and controller weights could also be carried out to further improve performance. Either way, it is clear that the MPC with re-linearisation, which uses a very small system description and with low computational cost in the updating process, offers very substantial advantages with respect to linear control architectures based on vehicle characteristics at the reference conditions.

We remark finally that the full-state feedback assumption should be replaced by a suitable observer of the modal amplitudes based on limited measurements. While this would affect both linear and nonlinear control strategies, the extent to which estimation of the nonlinear couplings may be affected by the estimation algorithm is an open question.
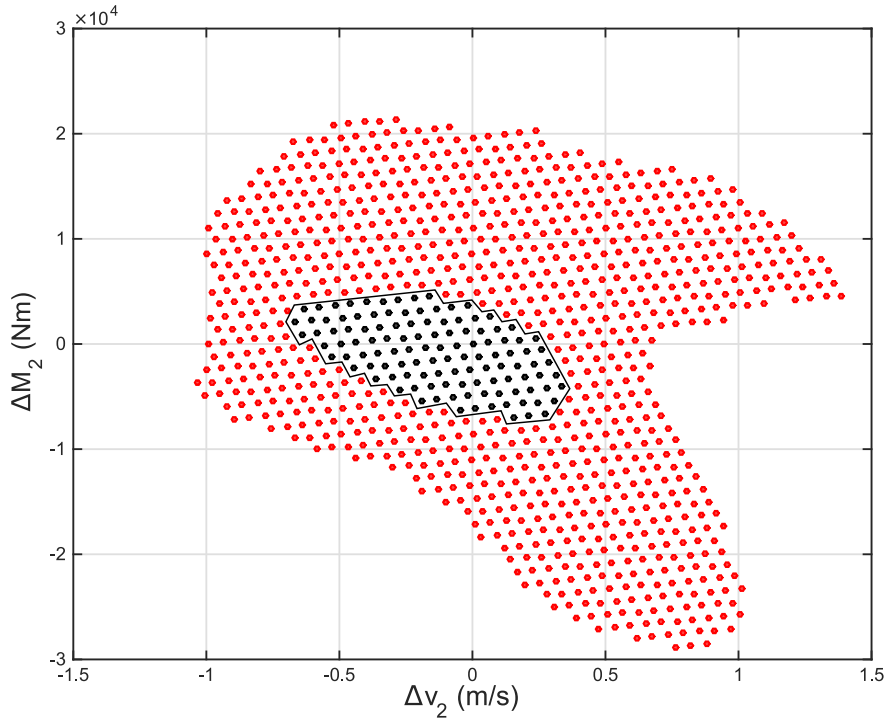
Figure 11. Stability regions of linear (black) and nonlinear (red) MPC when subject to combined initial excitations in longitudinal velocity and wing root bending moment.

3. MPC Trajectory Planning Results

In the previous section we have demonstrated that updating the internal model via successive re-linearisation can substantially increase the performance of the closed-loop system for large-amplitude disturbance rejection. We will investigate here the performance, and potential advantages, of the proposed nonlinear MPC for trajectory tracking. Two additional assumptions will be introduced to simplify the study. First, it will be assumed that there are no atmospheric disturbances; second, a relatively simple guidance algorithm will be used [22], which is schematically described in Figure 12: Given a reference trajectory, at every controller time step (as before, chosen here as Δt=0.2 s), the guidance algorithm identifies first a target point P at a given distance R_g along the trajectory. Then it commands a flight trajectory defined to be a circular arc projected in the horizontal plane and constant climb angle in the vertical plane, which intersects the reference trajectory at a target point P. This trajectory is then used to calculate a target angular velocity in the horizontal plane $\omega_T = 2V_\infty \sin\theta_T / d_T$, where θ_T is the angle in the horizontal plane between P and the aircraft heading angle, as shown in the figure, and d_T is the horizontal distance between P and the aircraft. The prescribed climb rate is $v_T = V_\infty h_T / d_T$ where h_T is the altitude difference between P and the aircraft, as shown in Figure 12. This simple two-part algorithm is selected as representative of that typically employed by a HALE-type aircraft [25]. Once the target horizontal angular velocity ω_T (which is limited to be below 0.1 rad/s) and climb rate v_T have been identified, they are converted to reference output and input trajectories $(\omega_T, v_T) \mapsto \{\mathbf{y}^{ref}, \mathbf{u}^{ref}\}$ to be employed in the MPC optimization (21) at current control time step T. The reference values $\mathbf{y}^{ref}$ and $\mathbf{u}^{ref}$ for

American Institute of Aeronautics and Astronautics

steady turns with fixed climb rate is obtained from a library of steady-state solutions to Eq. (2), and we note that the simplicity of the target trajectories renders such an approach practically feasible.
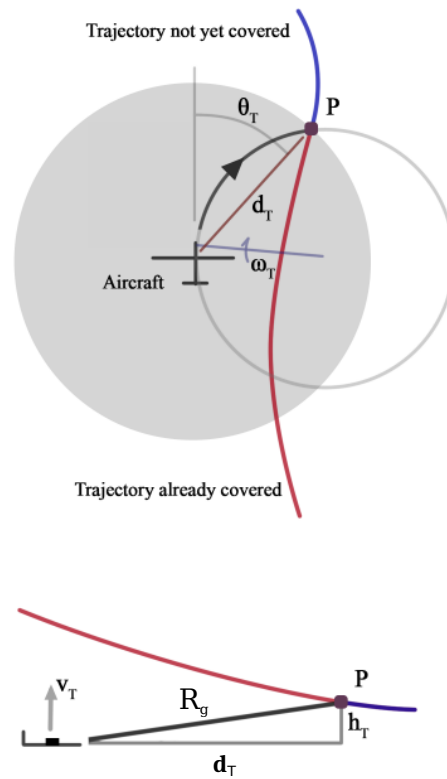

Figure 12.   Guidance algorithm: The target ω_T and v_T are computed based on the relative position of the target point P relative to the plane's current location.

For comparison, a nonlinear six-degrees-of-freedom (6DOF) MPC is developed based on a simplified internal model, which is obtained by retaining only the first six (rigid-body) modes in (2). Note that this model still includes nonlinear terms from the gyroscopic couplings and the gravitational forces, however, aeroelastic degrees of freedom are absent. Finally, as in the disturbance rejection problem studied above, a linear MPC, built around the reference trim condition, but without re-linearisation during the simulation, is also used to compare the performance of the re-linearisation technique.

In the numerical studies, the flight speed V_∞ is again set to 12.2m/s and the guidance radius R_g is set to 200 m, which defines a minimum turning radius of 100 m. Figure 13 shows the performance of the three different MPC controllers (nonlinear, linear, and nonlinear with 6DOF plant), in tracking circular horizontal trajectories with radii of 1000, 600, 400, 300, 250, 200 and 150m (the final case for the NL MPC only). For a large turning radius, the performance of all three controllers is identical as the response remains in the linear regime and with negligible aeroelastic effects. As the turning radius decreases, the nonlinear MPC manages to track the desired trajectory. The increasing differences between the actual and the reference trajectory are linked to the fixed value of R_g in the guidance

American Institute of Aeronautics and Astronautics

algorithm. The linear MPC controller, Figure 13b, overshoots the target turn rate as the radii become smaller. This initially has the effect of providing better tracking of the desired trajectory, but the vehicle eventually becomes unstable at a turn radius of 200 m. Finally, the 6DOF nonlinear MPC, Figure 13c, remains stable for all trajectories considered, however, it flies off-course for radii below 300 m. This can be linked to the absence of (nonlinear) aeroelastic couplings in the internal model.

a) Nonlinear MPC   b) Linear MPC   c) NL 6DOF MPC
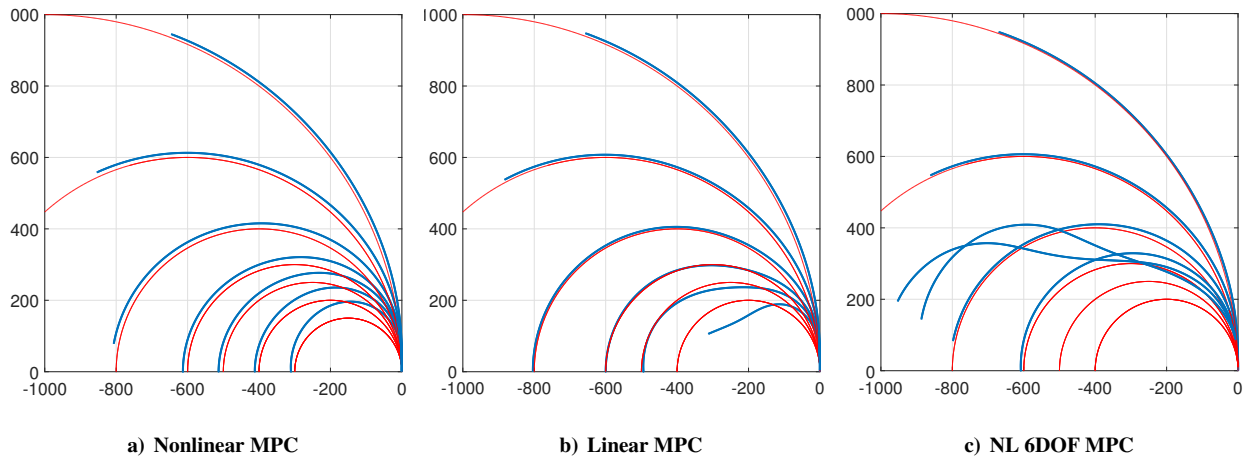
Figure 13. Tracking performance of MPC controllers of decreasing complexity for horizontal circular trajectories with radii ranging from 150 to 1000 m. (red: reference trajectories; blue: actual trajectories)

The ability of the nonlinear MPC to carry out tighter turns is further demonstrated in Figure 14, which shows a nominal and executed trajectory with the same initial conditions as above. The nominal trajectory is a square of side-length 1500 m in the horizontal plane. The trajectory is closely followed by the vehicle with a nonlinear MPC defined with a guidance radius $R_g = 200$ m, as before. Figure 15a provides a detailed view of the first commanded turn, which is also compared to the trajectory followed with the linear and 6DOF nonlinear MPC controllers. The commanded and actual horizontal turn rates (the angular velocity ω_T defined above) during this first turn are shown in Figure 15b for the three controllers. Finally, Fig. 16 shows all six input channels during the first commanded turn. As it can be seen, the linear and the 6DOF MPCs follow the same initial trajectory as the nonlinear MPC at the start of the turn, but perform poorly afterwards. In particular, the linear MPC, as it was seen for the previous case (Figure 13b), is not able to keep the vehicle stable as it enters the turn and the airframe eventually enters a divergent mode. The 6DOF MPC, on the other hand, includes rigid-body nonlinearities but not aeroelastic effects. This is sufficient to stabilise the phugoid even as the structure deforms, but the controller does not have sufficient information of the vehicle dynamics to effectively track the commanded trajectory. As it can be observed in Figure 15b, the commanded rate for this controller saturates as the aircraft turns and recovers only very slowly after that. The actual turn rate for the 6DOF MPC shows higher-frequency oscillations as the relatively fast turn excites the aeroelastic modes which are not known to the controller. Overall, the trajectory-tracking performance of the 6DOF has substantially degraded from

American Institute of Aeronautics and Astronautics

that of the proposed nonlinear MPC.

We should finally highlight that we have obtained the flight dynamics aerodynamic derivatives through a simple aerodynamic model and therefore the trajectory predictions will build cumulative errors, particularly in displacement and heading. The modal description, however, specifically identifies the states associated the rigid-body modes and corrections would be possible in the appropriate entries of the aerodynamic matrices in (9) if, e.g., flight test data were available.
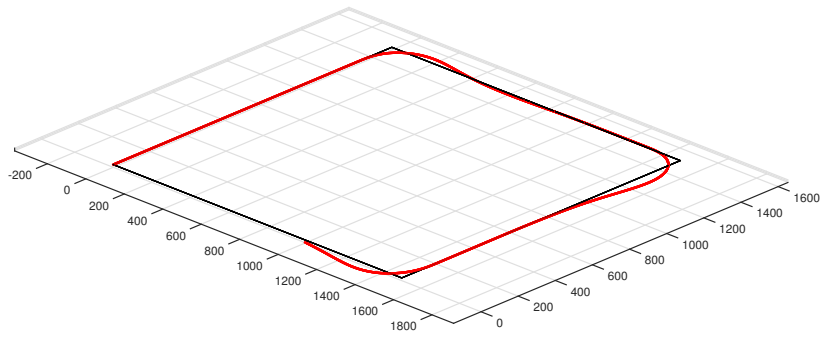

Figure 14.   Trajectory of the flying wing being guided along a square path (red) of size 1500m, controlled by the nonlinear MPC commanded by the trajectory-following algorithm.


a) **Reference and actual trajectories. In grey, the projection of the trajectories on the horizontal plane.**

b) **Commanded and actual horizontal turn rate, ω_T.**
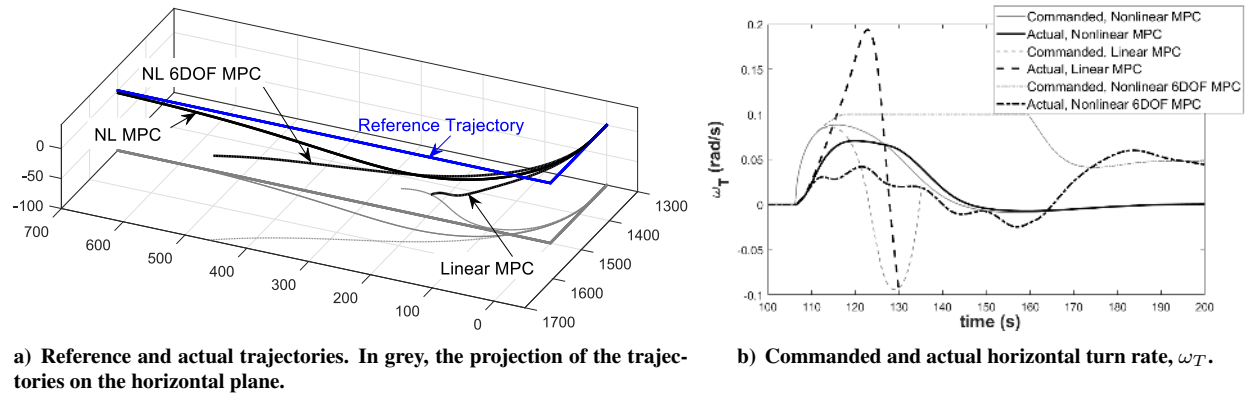
Figure 15.   Details of trajectory and angular velocity achieved by all three controllers during the first turn.

V.   Conclusions

We have demonstrated a strategy for nonlinear aeroservoelastic analysis of very flexible aircraft, which relies, first, on the effective generation of reduced-order models of the nonlinear flight dynamic/aeroelastic system, and, second, on an optimization-based controller that updates its internal model as the system evolves in time. By picking a structural
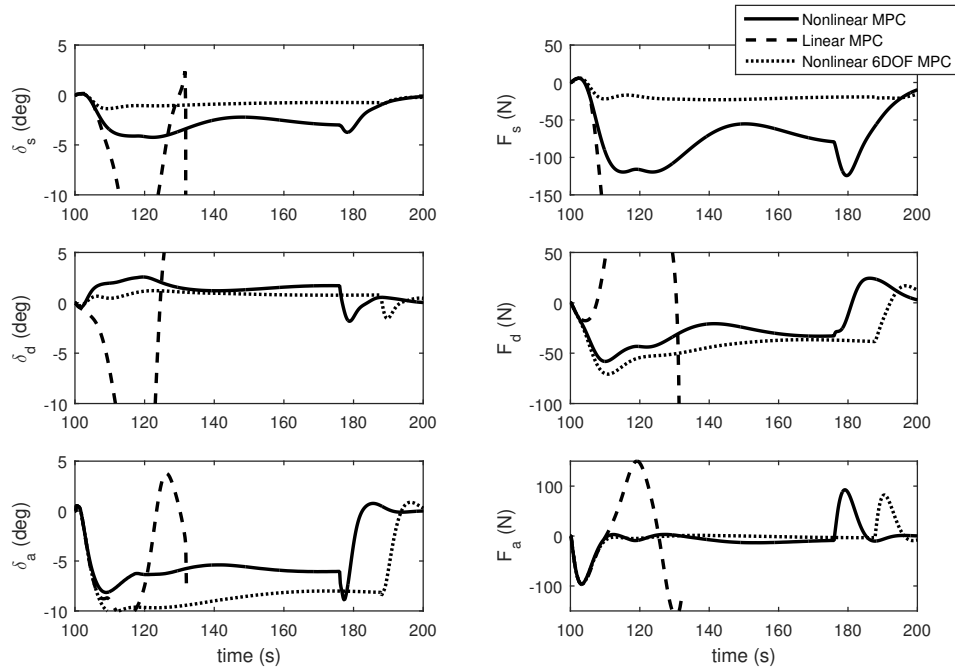
Figure 16. Input time histories for all three controllers during the first turn.

dynamics model that uses time and and spatial derivatives (velocities and internal forces) instead of displacements, the geometrically-nonlinear response has been represented with quadratic terms without any approximations. Furthermore, the formulation in velocities provides directly the instantaneous wall boundary conditions for the aerodynamic model. While a simple aerodynamic model has been chosen in this first implementation, more general modal-based unsteady aerodynamics descriptions (e.g. a doublet-lattice lifting surface model) could be easily integrated in the current description. It has been shown that a two-stage projection, first, on linear normal modes and, then, on balanced states, of the resulting nonlinear aeroelastic equations can characterise the main dynamics of the full aircraft with very few degrees of freedom. With improved aerodynamics, particularly for rigid-body aerodynamic derivatives, and a more computationally efficient implementation (the current implementation was built in Matlab), this framework may constitute a suitable platform for real-time flight simulation of very flexible aircraft.

A nonlinear model-predictive control based on rapid on-line re-linearisation of this reduced-order nonlinear model has been implemented and it has been demonstrated on a very flexible flying wing already investigated in the literature. In numerical test cases, the controller with a nonlinear plant model was able to achieve improved performance over an equivalent linear MPC in disturbance rejection and trajectory tracking scenarios. To facilitate this initial investigation, it has been assumed that the controller has full-state feedback and that all control inputs are below admissible thresholds without having to enforce saturation constraints in the optimization model. A rather simple navigation algorithm was also utilized. While removing either assumption will likely increase the computational demands on the online optimization, the nonlinear internal system required by the controller is of such small size that a successful real-time

implementation of the control system is still very likely to require only very modest computational resources. However, the physical implementation of the basic control scheme in this paper still requires the development of suitable observers of the nonlinear system dynamics.

VI. Acknowledgements

References

[1] F. Afonso, J. Vale, E. Oliveira, F. Lau, and A. Suleman. A review on non-linear aeroelasticity of high aspect-ratio wings. *Progress in Aerospace Sciences*, 89:40–57, feb 2017. doi:10.1016/j.paerosci.2016.12.004.

[2] R. M. Bertolin, F. J. Silvestre, A. B. Guimaraes Neto, G. C. Barbosa, P. J. Gonzalez, and C. E. S. Cesnik. Dynamic gain scheduling of highly flexible aircraft applying adaptive control. In *International Forum on Aeroelasticity and Structural Dynamics*, Como, Italy, June 2017.

[3] J.M Bravo, T. Alamo, and E. F. Camacho. Robust MPC of constrained discrete-time nonlinear systems based on approximated reachable sets. *Automatica*, 42(10):1745–1751, 2006. doi:10.1016/j.automatica.2006.05.003.

[4] C. E. S. Cesnik, R. Palacios, and E. Y. Reichenbach. Reexamined structural design procedures for very flexible aircraft. *Journal of Aircraft*, 51(5):1580–1591, 2014. doi:10.2514/1.C032464.

[5] C. S. Chang, D. H. Hodges, and M. J. Patil. Flight dynamics of highly flexible aircraft. *Journal of Aircraft*, 45(2):538–545, 2008. doi:10.2514/1.30890.

[6] R. G. Cook, R. Palacios, and P. Goulart. Robust gust alleviation and stabilization of very flexible aircraft. *AIAA Journal*, 51 (2):330–340, February 2013. doi:10.2514/1.j051697.

[7] M. J. Dillsaver, C. E. S. Cesnik, and I. V Kolmanovsky. Gust load alleviation control for very flexible aircraft. In *AIAA Atmospheric Flight Mechanics Conference*, Portland, Oregon, USA, 2011. AIAA Paper No. 2011-6368.

[8] M. J. Dillsaver, C. E. S. Cesnik, and I. V. Kolmanovsky. Gust response sensitivity characteristics of very flexible aircraft. In *AIAA Atmospheric Flight Mechanics Conference*, Minneapolis, Minnesota, 2012. AIAA Paper No. 2012-4576.

[9] M. J. Dillsaver, U. V. Kalabic, I. V. Kolmanovsky, and C. E. S. Cesnik. Constrained control of very flexible aircraft using reference and extended command governors. In *American Control Conference*, Washington, DC, USA, Jun 2013. doi:10.1109/acc.2013.6580065.

[10] G. Dimitriadis. *Introduction to Nonlinear Aeroelasticity*. Aerospace Series. John Wiley & Sons, Ltd, March 2017. doi:10.1002/9781118756478. Chapter 10.

[11] V. Duchaine, S. Bouchard, and C. M. Gosselin. Computationally efficient predictive robot control. *IEEE/ASME Transactions On Mechatronics*, 12(5):570–578, 2007. doi:10.1109/TMECH.2007.905722.

[12] H-G Giesseler, M Kopf, P Varutti, T Faulwasser, and R Findeisen. Model predictive control for gust load alleviation. In *4th IFAC Nonlinear Model Predictive Control Conference International Federation of Automatic Control*, Noordwijkerhout, The Netherlands, August 23-27 2012.

[13] S. Haghighat, J. R. R. A. Martins, and H. H. T. Liu. Model-predictive gust load alleviation controller for a highly flexible aircraft. *Journal of Guidance, Control, and Dynamics*, 35(6):1751–1766, November 2012. doi:10.2514/1.57013.

[14] M. A. Henson. Nonlinear model predictive control: current status and future directions. *Computers & Chemical Engineering*, 23(2):187–202, 1998. doi:10.1016/S0098-1354(98)00260-9.

[15] D. H. Hodges. Geometrically exact, intrinsic theory for dynamics of curved and twisted anisotropic beams. *AIAA Journal*, 41 (6):1131–1137, 2003. doi:10.2514/2.2054.

[16] S. Hosseini and M. Mesbahi. Energy-aware aerial surveillance for a long-endurance solar-powered unmanned aerial vehicles. *Journal of Guidance, Control, and Dynamics*, 39(9):1980–1993, sep 2016. doi:10.2514/1.G001737.

[17] A. Ilzhöfer, B. Houska, and M. Diehl. Nonlinear mpc of kites under varying wind conditions for a new class of large-scale wind power generators. *International Journal of Robust and Nonlinear Control*, 17(17):1590–1599, 2007. doi:10.1002/rnc.1210.

[18] A. T. Klesh and P. T. Kabamba. Solar-powered aircraft: Energy-optimal path planning and perpetual endurance. *Journal of Guidance, Control, and Dynamics*, 32(4):1320–1329, 2009. doi:10.2514/1.40139.

[19] Joseba Murua, Rafael Palacios, and J Michael R Graham. Applications of the unsteady vortex-lattice method in aircraft aeroelasticity and flight dynamics. *Progress in Aerospace Sciences*, 55:46–72, November 2012.

[20] R. Palacios. Nonlinear normal modes in an intrinsic theory of anisotropic beams. *Journal of Sound and Vibration*, 330(8): 1772–1792, April 2011. doi:10.1s016/j.jsv.2010.10.023.

[21] R. Palacios, J. Murua, and R. G. Cook. Structural and aerodynamic models in nonlinear flight dynamics of very flexible aircraft. *AIAA Journal*, 48(11):2648–2659, 2010. doi:10.2514/1.J050513.

[22] S. Park, J. Deyst, and J. P. How. Performance and Lyapunov stability of a nonlinear path following guidance method. *Journal of Guidance, Control, and Dynamics*, 30(6):1718–1728, nov 2007. doi:10.2514/1.28957.

[23] M. J. Patil and D. H. Hodges. Flight dynamics of highly flexible flying wings. *Journal of Aircraft*, 43(6):1790–1799, 2006. doi:10.2514/1.17640.

[24] D. A. Peters. Two-dimensional incompressible unsteady airfoil theory–an overview. *Journal of Fluids and Structures*, 24(3): 295–312, 2008. doi:10.1016/j.jfluidstructs.2007.09.001.

[25] B. Raghavan and M. J Patil. Flight control for flexible, high-aspect-ratio flying wings. *Journal of Guidance, Control, and Dynamics*, 33(1):64–74, 2010. doi:10.2514/1.45471.

[26] J. B. Rawlings and D. Q. Mayne. *Model Predictive Control: Theory and Design*. Nob Hill Publishing, 2009.

[27] C. M. Shearer and C. E. S. Cesnik. Trajectory control for very flexible aircraft. *Journal of Guidance, Control, and Dynamics*, 31(2):340–57, mar 2008. doi:10.2514/1.29335.

[28] J.J.E. Slotine and W. Li. *Applied Nonlinear Control*. Prentice-Hall Englewood Cliffs, NJ, 1991.

[29] W. Su and C. E. S. S. Cesnik. Dynamic response of highly flexible flying wings. *AIAA Journal*, 49(2):324–339, 2011. doi:10.2514/1.J050496.

[30] Y. Wang, R. Palacios, and A. Wynn. A method for normal-mode-based model reduction in nonlinear dynamics of slender structures. *Computers & Structures*, 159:26–40, 2015. doi:10.1016/j.compstruc.2015.07.001.

[31] Y. Wang, A. Wynn, and R. Palacios. Nonlinear modal aeroservoelastic analysis framework for flexible aircraft. *AIAA Journal*, 54(10):3075–3090, oct 2016. doi:10.2514/1.j054537.

[32] Z. Wang, P. C. Chen, D. D. Liu, and D. T Mook. Nonlinear-aerodynamics/nonlinear-structure interaction methodology for a high-altitude long-endurance wing. *Journal of Aircraft*, 47(2):556–566, 2010. doi:10.2514/1.45694.

American Institute of Aeronautics and Astronautics